AIAA SciTech Forum
6-10 January 2025, Orlando, FL
AIAA SCITECH 2025 Forum

10.2514/6.2025-1111

Stability Investigations of Mach 5.35 Boundary Layer Flow Over Distributed Roughness

Sean Dungan*, Bijaylakshmi Saikia† and Christoph Brehm‡
University of Maryland, College Park, MD, 20742, USA

Stability analysis of Mach 5.35 boundary layer flow over a flat plate with two- and three-dimensional sinusoidal roughness is performed and presented. The impact of the distributed roughness amplitude is shown for the second Mack mode, which is the dominant instability for this flow condition. It is found for all roughness heights examined that the second Mack mode is appreciably destabilized relative to the smooth wall flat plate. An energy budget analysis was performed for a selected roughness case and compared with the smooth wall. It was shown that the primary mechanism for destabilization of the second mode in the roughness case is heightened Reynolds stress energy production owing to the compression-expansion shock wave system formed by the roughness elements peaks. Decreased (relative to the smooth wall) disturbance energy dissipation via heat conduction caused by the separated flow over the roughness trough combined to contributed to the destabilization as well. Finally, the same 2-D roughness surface when extended into 3-D showed even larger destabilization of 2-D waves.

I. Introduction

Boundary transition (BLT) from laminar flow to turbulence at high speeds persists as a state-of-the-art fluid dynamics research problem. Its importance stems from the nearly order of magnitude increase in heat flux imparted on a vehicle's surface when subjected to turbulent rather than laminar flow [1]. Being able to predict where this stark difference occurs over the vehicle is very important to vehicle designers. Making matters worse, the highly nonlinear regime of boundary layer transition preceding turbulence has been shown to introduce heating overshoots that are significantly higher than those predicted in the turbulent regime [2]. Of the many challenges associated with predicting and understanding BLT, surface roughness presents one of the largest spaces of unknowns. Many numerical studies have previously been performed considering high-speed flow over isolated/discrete roughness elements, a small sampling of which include Refs. 3,4,5, 6. Counter-rotating vortices form downstream of the isolated roughness elements when the roughness element height is comparable with the local boundary layer height and result in velocity streaks. Without subsequent roughness elements downstream, the streaks are able to cleanly evolve over the smooth wall. These effect the stability of the boundary layer two ways: (1) through the modification of the dominant boundary layer mode of the otherwise smooth wall flow, and (2) through the generation (given sufficient roughness element height) of wake instability modes. Since the wake modes behind the discrete roughness element derive energy from the wall-normal and/or spanwise shear introduced by the velocity streaks, the type and growth rate of the wake modes are highly dependent on the roughness element's geometry and orientation [7].

In many applications, however, the roughness elements cover the entire vehicle's surface. Much less is known about BLT in this case. Numerical solution becomes prohibitively expensive if all roughness scales are to be resolved. Thus, approximations to the typically randomly distributed surface topology are necessary. A popular roughness approximation taken by several previous works is to use sinusoidal distributions for roughness elements [8, 9]. Governing parameters for the sinusoidal shape (amplitude and wavelength) were varied parametrically for the case of two-dimensional (2-D) flat plate boundary layer flow at Mach 5.35 in Refs. 10,11,12. While not completely distributed, Chou et al. [13] looked at a 3-D sinusoidal roughness patch on a flat plate in Mach 3.5 flow. Similar to the isolated roughness cases, the effects of the roughness were mainly in the wake of the patch. Recently, Braga et al. [14] simulated distributed sinusoidal roughness over the surface of a cylinder at Mach 6. The results qualitatively resembled the experiments performed by Hollis [15] and highlighted that the most amplified convective mode was two-dimensional, bearing a strong resemblance to a Tollmien-Schliching wave. The exact mechanism governing the transition process proved allusive given the complicated roughness element-wake interactions, accelerating flow, and possibility of global instabilities.

*Ph.D. Candidate, Aerospace Engineering, 3179 Glenn L. Martin Hall Bldg. sdungan@umd.edu
†Postdoctoral Researcher, Aerospace Engineering, 3179 Glenn L. Martin Hall Bldg., Member AIAA.
‡Associate Professor, Aerospace Engineering, 3179 Glenn L. Martin Hall Bldg. cbrehm1@umd.edu, Member AIAA

Thus, in the view of the authors, it appears the proper means by which realistic surface roughness can be incorporated into tractable numerical solutions and physics-based engineering tools remains largely unknown.

Recent work [16] analyzed two-dimensional surface roughness effects on second Mack mode growth and serves as the basis for this paper. This manuscript is organized in the following way. First, the numerical approach for solution is presented in Section II, followed by the simulation setup including flow conditions and roughness generation in Section III. Next, key differences between the rough and smooth wall mean and disturbance flow fields are highlighted in Sections IV and V, respectively. An energy budget analysis is then performed in Section VI to better understand the different mechanisms governing disturbance growth for the 2-D cases. Finally, steps are taken to include three-dimensionality in the analysis in Section VII. Conclusions are presented last.

II. Numerical Method

The dynamics of a single species, Newtonian, perfect gas are known to be governed by the Navier-Stokes equations (NSE) given below in Eq. 1 written in the Cartesian coordinate system (x, y, z).

$$\frac{\partial \mathbf{W}}{\partial t} = \frac{\partial \mathbf{E}}{\partial x} + \frac{\partial \mathbf{F}}{\partial y} + \frac{\partial \mathbf{G}}{\partial z} \tag{1}$$

The conserved state vector along with the flux vectors are defined below in Eq. 2.

$$\mathbf{W} = \begin{bmatrix} \rho \\ \rho u \\ \rho v \\ \rho w \\ \rho E_t \end{bmatrix}, \mathbf{E} = \begin{bmatrix} \rho u \\ \rho u^2 + p - \tau_{xx} \\ \rho uv - \tau_{xy} \\ \rho uw - \tau_{xz} \\ (\rho E_t + p)u - u\tau_{xx} - v\tau_{xy} - w\tau_{xz} + q_x \end{bmatrix},$$
$$\mathbf{F} = \begin{bmatrix} \rho v \\ \rho uv - \tau_{xy} \\ \rho v^2 + p - \tau_{yy} \\ \rho vw - \tau_{yz} \\ (\rho E_t + p)v - u\tau_{xy} - v\tau_{yy} - w\tau_{yz} + q_y \end{bmatrix}, \mathbf{G} = \begin{bmatrix} \rho w \\ \rho uw - \tau_{xz} \\ \rho vw - \tau_{yz} \\ \rho w^2 + p - \tau_{zz} \\ (\rho E_t + p)w - u\tau_{xz} - v\tau_{yz} - w\tau_{zz} + q_z \end{bmatrix} \tag{2}$$

The variables ρ, u, v, w, p, and E_t are the density, velocity components in the Cartesian coordinate system, pressure, and total specific energy, respectively. Total specific energy is the summation of internal and kinetic energy: $E_t = e + u_i u_i/2$, using repeated index notation to denote summation. The shear-stress tensor, τ, has components

$$\begin{aligned} \tau_{xx} &= \tfrac{2\mu}{3}\left(2\tfrac{\partial u}{\partial x} - \tfrac{\partial v}{\partial y} - \tfrac{\partial w}{\partial z}\right) \\ \tau_{yy} &= \tfrac{2\mu}{3}\left(2\tfrac{\partial v}{\partial y} - \tfrac{\partial u}{\partial x} - \tfrac{\partial w}{\partial z}\right) \\ \tau_{zz} &= \tfrac{2\mu}{3}\left(2\tfrac{\partial w}{\partial z} - \tfrac{\partial u}{\partial x} - \tfrac{\partial v}{\partial y}\right) \\ \tau_{xy} &= \mu\left(\tfrac{\partial u}{\partial y} + \tfrac{\partial v}{\partial x}\right) \\ \tau_{xz} &= \mu\left(\tfrac{\partial u}{\partial z} + \tfrac{\partial w}{\partial x}\right) \\ \tau_{yz} &= \mu\left(\tfrac{\partial v}{\partial z} + \tfrac{\partial w}{\partial y}\right) \end{aligned} \tag{3}$$

and the heat-flux vector has components

$$q_x = -\kappa\frac{\partial T}{\partial x} \quad q_y = -\kappa\frac{\partial T}{\partial y} \quad q_z = -\kappa\frac{\partial T}{\partial z}. \tag{4}$$

The dynamic viscosity, μ, of the gas is modeled with Sutherland's law, and the thermal conductivity, κ, is computed, assuming a constant Prandtl number of $Pr = 0.72$, as

$$\kappa = \frac{\mu R_{gas}\gamma}{Pr(\gamma - 1)} \tag{5}$$

The system is closed with the perfect gas equations of state ($P = \rho R_{gas} T$).

Given the low disturbance amplitudes assumed for natural transition, early stages of BLT can be studied by solving the linearized Navier-Stokes equations (LNSE), whereby a disturbance field of flow variables superimposed on an underlying mean flow that satisfies the full NSE is solved for. Thus, the total state vector $\mathbf{W}$, is assumed to be the summation of a mean, $\bar{\mathbf{W}}$, and a fluctuating state, $\mathbf{W}'$. Substituting this decomposition into Eq. 1 and subtracting out the mean flow (assumed to identically satisfy the NSE), the LNSE equations are obtained.

$$\frac{\partial \mathbf{W}'}{\partial t} = \frac{\partial \mathbf{E}'}{\partial x} + \frac{\partial \mathbf{F}'}{\partial y} + \frac{\partial \mathbf{G}'}{\partial z} \tag{6}$$

The convective portion of this linear flux in the x-direction, for example, is given below in Eq. 7

$$\mathbf{E}'_{\mathbf{c}} = \begin{bmatrix} \bar{\rho}u' + \rho'\bar{u} \\ 2\bar{\rho}\bar{u}u' + \rho'\bar{u}^2 + p' \\ \bar{\rho}\left(\bar{u}v' + u'\bar{v}\right) + \rho'\bar{u}\bar{v} \\ \bar{\rho}\left(\bar{u}w' + u'\bar{w}\right) + \rho'\bar{u}\bar{w} \\ \left(\rho'\bar{E}_t + \bar{\rho}E'_t + p'\right)\bar{u} + \left(\bar{\rho}\bar{E}_t + \bar{p}\right)u' \end{bmatrix}, \tag{7}$$

where all products of fluctuating quantities have been assumed to be negligibly small. Disturbances can be introduced to the field through a source term, $\mathbf{S}$, making Eq. 6 take the form

$$\frac{\partial \mathbf{W}'}{\partial t} = \mathbf{R}' + \mathbf{S} \tag{8}$$

where the spatial derivatives have been grouped into the LNSE right-hand-side vector, $\mathbf{R}'$. The LNSE were solved in the generalized curvilinear coordinate system following [17]. For the sake of brevity, the equations above were written in the Cartesian frame. The reader is directed to Ref. 18, 19 for more details on the LNSE solver solving the disturbance flow equations both in the time and frequency domains.

III. Simulation Setup

A. Flow Condition

The steady, mean field is computed for a Mach 5.35 flow over an adiabatic flat plate at a free stream temperature of 64.316 K and a unit Reynolds number of 14.356×10^6 1/m. This flow condition produces a boundary layer with edge quantities very similar to those of the 7-degree sharp cone used in the Boeing/AFOSR Mach 6 quiet-flow Ludwieg Tube at Purdue University.

B. Roughness Generation

Roughness is introduced at the wall using the following equation:

$$y_{rough} = y_{smoooth} - A f(x) g(x, z). \tag{9}$$

where

$$f(x) = \frac{1}{2}\left[cos\left(\frac{2\pi(x - x_s)}{\lambda_x}\right) - 1\right] \tag{10}$$

and

$$g(x, z) = \begin{cases} \frac{1}{2}\left[cos\left(\frac{2\pi z}{\lambda_x} + \phi_r(x)\right) - 1\right] & \text{if } \mathbf{W} = \mathbf{W}(x, y, z) \\ 1 & \text{if } \mathbf{W} = \mathbf{W}(x, y) \end{cases} \tag{11}$$

The shape function in x-direction was identical to the form used in Ref. 16, except for the 3-D calculations where the mesh was perturbed upward (i.e., $A \rightarrow -A$) rather than downward like for the 2-D calculations. The dependence of the solution on this choice appears minimal in terms of disturbance growth rate, however, the receptivity process is noticeably altered (see Appendix VIII.B). Perturbing the mesh upward allowed a larger initial time step size to be taken and decreased computational resources consumed by 3-D calculations. The starting location of the roughness, x_s, was

set to $x_s = 0.026$ m. The shape function in the z-(span-) direction is of a similar functional form with the addition of a random variable $\phi(x)$ applied to randomize the distribution of roughness element peaks. The random variable is written as a continuous function of x, but was implemented by binning the randomized phase precisely by λ_x such that the surface topology remained in C^1. Previous work [11] swept the amplitude (A) space listed in Table 1. The parameters for the case W2A3 are the focus of the majority of the analysis presented here, namely a $\lambda_x = 8$ mm and $A = 1.5$ mm. Each roughness element was resolved with 64 cells in the stream-wise direction and an initial wall spacing of $\Delta y_w = 8$ μm was used. This mesh resolution was verified in Appendix VIII.A to be sufficient for 2-D disturbance calculations. These parameters were also utilized in the 3-D calculations.

Cases	Wavelength, λ_x (mm)	λ_x/λ_{2nd}	Amplitude, A (mm)
W1A2	4	0.44	0.96
W2A2	8	0.89	0.96
W3A2	16	1.78	0.96
W4A2	32	3.56	0.96

Table 1 Test cases from Ref. 16 constructed to study the effects of varying 2-D roughness height on second mode instability growth.

IV. Steady Field

The steady flow field (sometimes referred to as "mean") over the 2-D flat plates with sinusoidal roughness were computed using a first-order backward differentiation formula (BDF) implicit scheme to drive the residual of the compressible Navier-Stokes equations toward zero over the domain of interest.[20] For the convective terms a fifth-order accurate blended WENO scheme[21] and a second-order centered scheme for the viscous terms were chosen. Convergence was obtained once the maximum residual of the energy equation dropped below a threshold criteria inside the boundary layer, here taken as 10^{-6}. Previous work [11] showed that the roughness elements are of sufficient height as to generate a compression (expansion) shock system in the vicinity of the roughness windward (leeward) peak. In addition, the combination of the compression shock's adverse pressure gradient and the turning curvature of the wavy wall causes the boundary layer to separate from the wall over the trough of the roughness element. Roughness-element averaged mean field wall-normal profiles (nondimensionalized using the local viscous length scale $\eta = y/H$, $H = [(\mu_\infty x)/(\rho_\infty u_\infty)]^{1/2}$) shown in Figure 1 highlight the velocity profiles becoming increasingly inflectional (height where $\partial\bar{u}/\partial y$ changes sign increases) as the extent and strength of the flow separation increases with roughness element height. The temperature profiles obtained in the same way shown in Figure 1 portray less of an effect. There is a slight increase in adiabatic wall temperature accompanying the increase in roughness element height. The most noticeable effect is the increase in effective boundary layer height with increasing roughness height. Measured from $y = 0$, the boundary layer height, δ_{99}, where $\bar{u}/u_\infty = 0.99$, remains nearly the same in all cases. Averaging over a roughness wavelength where the y coordinate dips below zero increases the δ_{99} at each location, which in turn increases the value emerging from the average. This difference becomes important for how disturbances propagate and grow in the boundary layer, especially for the most amplified second Mack mode that is tuned to the local value of δ_{99}.

V. Disturbance Field

With a steady state solution obtained, a Gaussian (in time) pulse disturbance in the wall-normal momentum equation was introduced upstream of the beginning of the roughness over a stream-wise width of $x \in [0.02, 0.023]$ m. The linearized Navier-Stokes equations (LNSE) were then used to propagate the pulse in time and space. Once the pulse disturbance had fully propagated through the domain, the pressure disturbance signal at the wall (P_w) was projected onto the temporal Fourier basis using the fast Fourier Transform (FFT). Performing this projection for each stream-wise location allows one to visualize the disturbance spectra development as shown in Figure 3. Beginning with the smooth wall case, hereafter referred to as "FP", one can see that disturbances within a particular frequency band experience downstream amplification. At these free-stream conditions and Mach number, this family of disturbances is referred to as Mack's second mode [22]. Visuals of the pressure field as shown in the right of Figure 2 confirm it is the second mode given the classic "two-cell" structure. The interpretation of this disturbance wave as a resonating acoustic wave

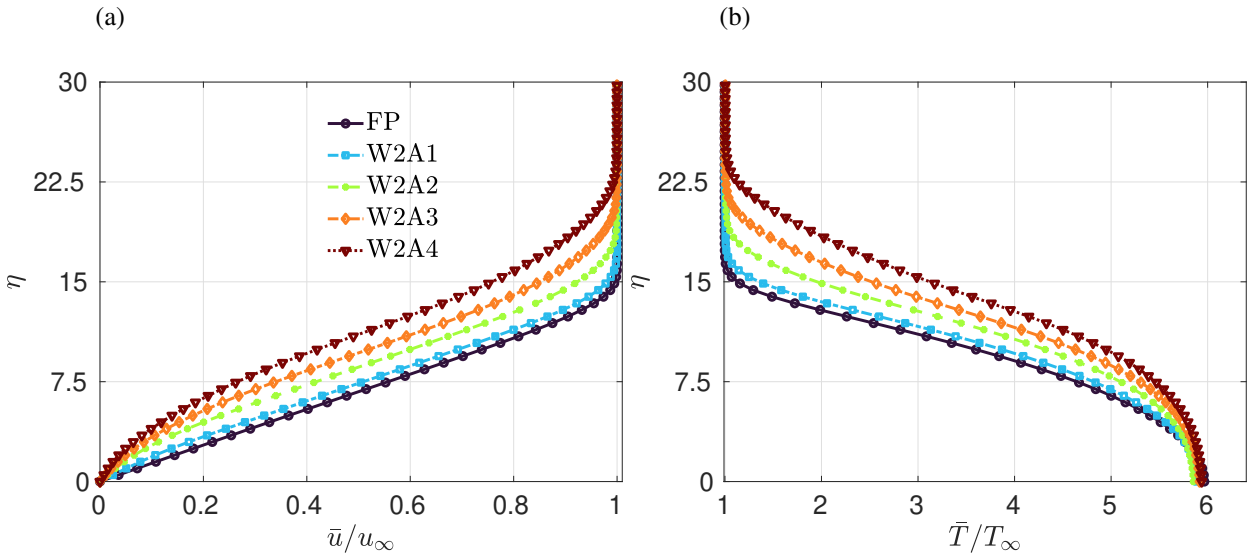

Fig. 1 Streamwise velocity (a) and temperature (b) wall-normal profile comparison between smooth and 2-D rough wall.

trapped in the acoustic impedance well formed by the wall and sonic line means that the most amplified frequency follows roughly twice the local boundary layer thickness [23]. For a smooth wall flat plate boundary layer, the boundary layer edge height grows proportionally to the square root of the stream-wise location ($\delta_{99} \propto \sqrt{x}$). The effect of this is shown in Figure 3a where the lower neutral curve (barrier between white and color at the bottom of the unstable frequency band) seems to follow inversely proportion to $\sqrt{x}$.

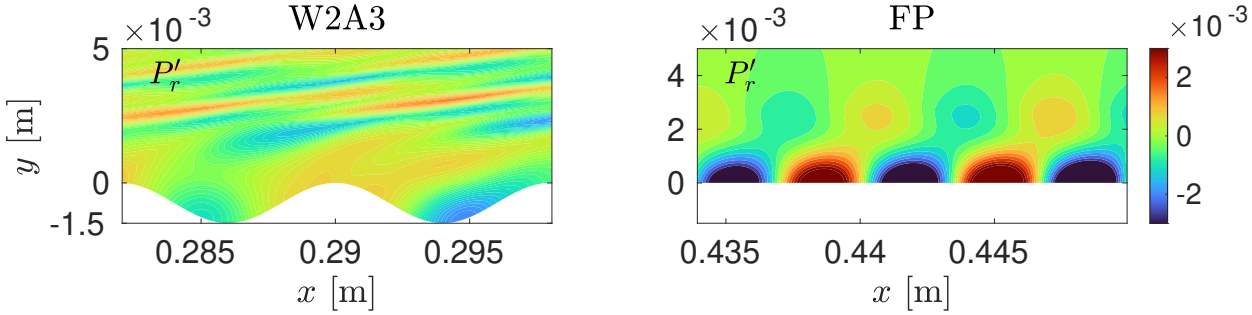

Fig. 2 Real part of disturbance pressure field for FP (flat plate) and 2-D roughness case W2A3.

Several important differences arise when roughness is introduced at the wall, which is shown in Figure 3b and Figure 3c for cases W2A1 and W2A3, respectively. For smaller roughness height (W2A1), the frequency band experiencing instability is slightly enlarged and the maximum amplitude reached in the domain is increased as compared to the smooth wall. Increasing the roughness height even more results in the emergence of two bands of unstable frequencies that merge into one in the downstream direction (see Figure 3c). The lower frequency of the two was shown to still be Mack's second mode [16], even though a glance at the disturbance field (left of Figure 2) would not immediately convey this fact. The higher frequency lobe in Figure 3c corresponds to Mack's third mode. That higher Mack modes can become destabilized by local flow separation was also seen in the flow field around the cone-cylinder-flare geometry [24]. While it is interesting to note that roughness can destabilize Mack's third mode, its even larger destabilizing effect on the second mode is most important in this case to boundary layer transition since the second mode reaches the highest amplitude within the domain. The destabilized second modes are also shifted to lower frequency for the roughness case, which can be attributed to the increased effective boundary layer height mentioned previously. Not only are the frequencies lower, but the neutral curve for the roughness case varies less strongly with x than the FP case, suggesting that the effective boundary layer height no longer follows $\sqrt{x}$ anymore.

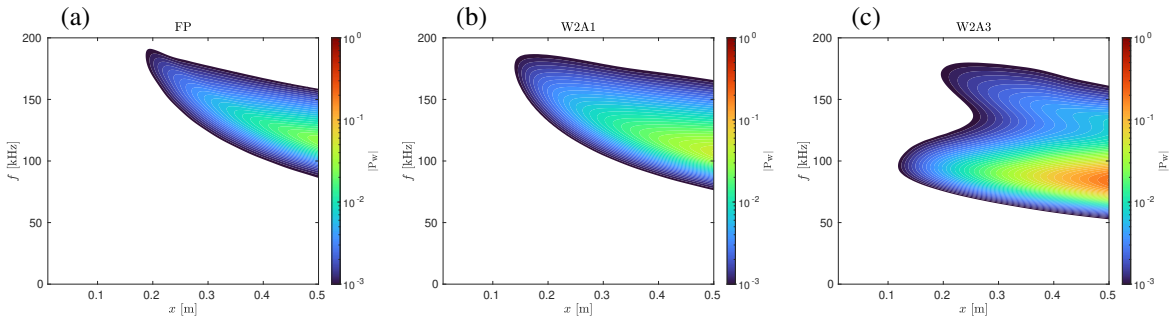

Fig. 3 Wall pressure disturbance spectra for (a) flat plate, (b) W2A1 and (c) W2A3.

Normalizing the wall pressure amplitude by the wave's amplitude at the neutral curve (x_{nc}) yields the commonly used "N factor" (N) for evaluating relative growth of disturbances in the boundary layer: $N = ln\,[P_w(x)/P_w(x = x_{nc})]$. These N factors, plotted in Figure 4 for the unstable frequency band previously highlighted in the spectra, give a more detailed view of the disturbance amplification. Among the range of unstable frequencies for the FP case (see Figure 4a), the one that reaches its peak by the end of the domain in consideration ($x = 0.5$) is $f = 116$ kHz and results in an appreciable $N \approx 6$ (transition historically predicted to occur when N reaches 9 [25]). Similarly, N factor curves for the band of unstable frequencies for roughness case W2A3 are shown in Figure 4b. Here the previously mentioned downward shift in frequency of the most unstable second mode can be seen with a frequency $f = 78$ kHz corresponding to the maximum N factor reached in the domain. At $N \approx 7.2$, it is clear that the second mode has been destabilized by nearly 20%. If one's transition criteria were $N = 6$, then the transition location (x_{tr}) for case W2A3 would be $x_{tr} = 0.375$ m, a 25% percent decrease from $x_{tr} = 0.5$ for the FP case. Destabilization of the second mode was obtained for the other roughness height cases as well (W2A1, W2A2, W2A4) and their N factor envelopes (taking max N over all f for each x) are plotted along with cases FP and W2A3 in Figure 4c. Using this $N = 6$ transition criteria again just for example, one would conclude that transition would occur most upstream for the lowest amplitude case W2A1 and each successive roughness height would transition later than the previous, followed lastly by the smooth wall case (FP).

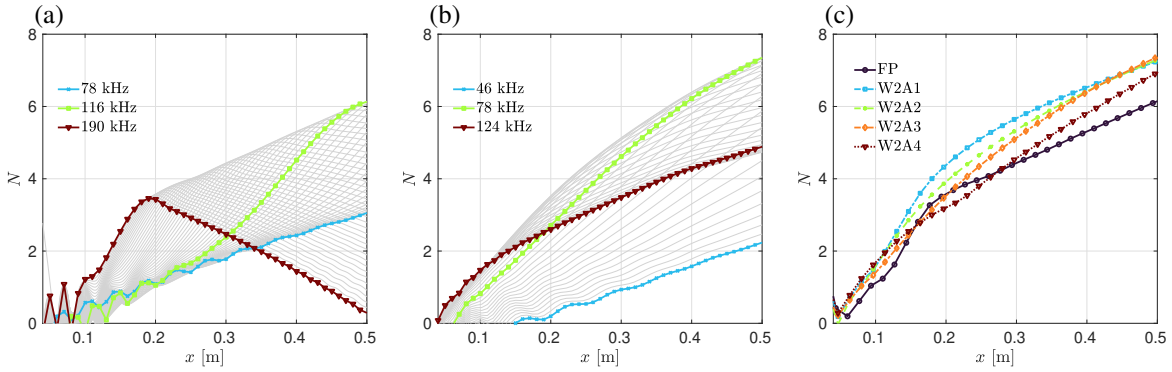

Fig. 4 N factor development in the stream-wise direction for (a) smooth wall and (b) W2A3, and (c) envelope comparison between the cases.

The LST code of Tumin [26] was used in Ref. 16 to help show the disturbances propagating over the roughness wall were indeed second mode. It is clear to the authors that the fundamental assumption underlying LST, quasi-parallel boundary layer flow, is severely violated for boundary layer flow over the roughness considered here. Despite this, LST proved useful not only for modal classification but also for identifying length scales to collapse growth rate distributions in the dimensionless frequency space. Nondimensionalizing frequency using the local boundary layer height (δ_{99}) provided a good collapse for some but not all locations analyzed along the roughness element wavelength. Trying the local sonic line height only slightly improve the scaling. It was shown that the correct length scale to collapse the data was the wavelength of the maximum amplification second mode at each location. Using this length scale, Figure 5a for case W2A3 shows how the peaks corresponding to both the second and third mode all occur at the same dimensionless frequency $F_\lambda = f u_\infty / \lambda_{2nd,max}$. The x locations of $x = 0.3980$ m and $x = 0.3992$ m correspond to roughness troughs,

whereas the $x = 0.4016$ m location is on a roughness peak. Such a scaling is important for providing estimates of peak amplification frequencies over rough walls, analogous to the rule of thumb that the second mode frequency roughly follows $f_{2nd} \approx 0.9u_\infty/(2\delta_{99})$ for the smooth wall case. In addition, the growth rate output from performing LST calculations at each wall-normal location, when averaged over a roughness element wavelength λ_x, compare surprisingly well with the wavelength-averaged growth rate obtained by solving the full LNSE. This (at least qualitatively) decent agreement for both the second and third mode peaks in growth rate-frequency space are shown at $x = 0.4$ m for the W2A3 case in Figure 5b. Such agreement suggest that, even if the intermediate stages of disturbance development over a roughness element wavelength are not perfectly captured by LST, LST might be able capture the average developments. Using LST outside of its domain of applicability is taken one step further in Figure 5c. Here, the wavelength-averaged mean field wall-normal profiles (previously highlighted in Figure 1) are used to compute the LST and linear parabolized stability equations [27] growth rates using the LASTRAC software [28]. Past the receptivity region ($x \in [0.02, 0.4]$ m), the growth rate from the LNSE calculation compares surprisingly "well" with those predicted by LST and LPSE, with slightly better agreement being found with LST than LPSE, which is probably for the wrong reasons. A result like this, though, suggests that the wavelength-averaged flow field is sufficient to get roughly the correct amplification rate for second mode disturbances over 2-D roughness. The advantage of using LST or LPSE is, of course, the tremendously lower computational resources required to solve the problem than using the LNSE.

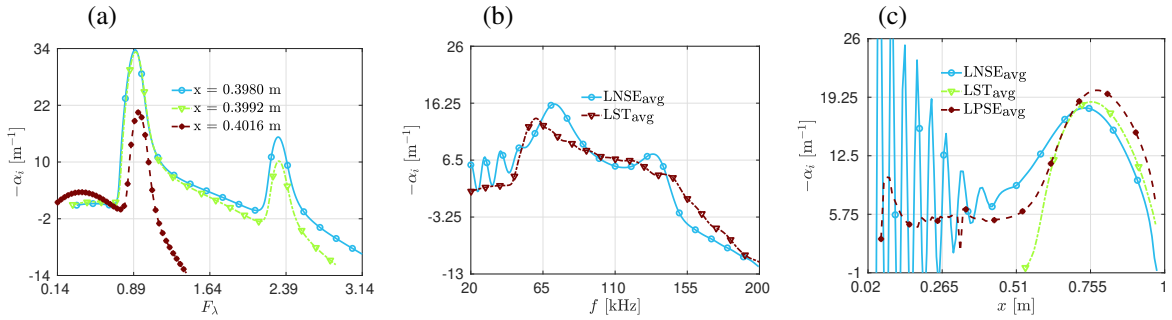

Fig. 5 (a) Second mode growth rate plotted versus nondimensionalized frequency using second mode wavelength (W2A3), (b) Averaged LST over roughness wavelength compared to LNSE growth rate at $x = 0.4$ m (W2A3), and (c) growth rate stream-wise development comparison for local analysis versus LNSE (W2A1) for $f = 78$ kHz.

VI. Energy Budget Analysis

This section seeks to understand why the 2-D roughness introduced at the wall destabilizes the second mode compared to the smooth wall case. To do this, an energy budget analysis is performed the same way as in Montero & Pinna [3] and Russo et al. [29]. This approach uses the Chu energy norm [30] to derive the equation governing the growth rate of disturbance energy in the stream-wise direction. In Ref. 29 this type of analysis was able to explain why the second mode was more unstable when presented with CO_2 injection gas rather than air. It was shown the destabilization mechanism stems from a reduction in dissipation (caused by lower thermal conductivity for CO_2) rather than a notable increase in energy production — an unexpected result that might have been overlooked by studies primarily focusing on energy production mechanisms.

It is well-know and has been highlighted in various prior works that Chu's energy norm is not consistent for the spatial problem [31]. The reader is referred to Ref. 29 for all the energy budget terms since only the necessary ones are presented here for the sake of brevity. Following Russo et al. [29], the total growth rate of disturbance energy $\alpha_{i,E}$ at each stream-wise location can be computed by

$$\alpha_{i,E}(x) = \frac{\int_{y=0}^{y\to\infty} \mathrm{P_{tot}}(x,y) + \mathrm{F_{tot}}(x,y) + \mathrm{D_{tot}}(x,y)\, dy}{\int_{y=0}^{y\to\infty} -2\bar{u}(x,y)E'(x,y)\, dy}. \tag{12}$$

In Eq. 12, the terms $\mathrm{P_{tot}}$,$\mathrm{F_{tot}}$, and $\mathrm{D_{tot}}$ represent the total disturbance energy production, flux (redistribution), and dissipation terms. The disturbance energy as defined by Chu [30] is given by

$$E' = \frac{1}{2}\left(\frac{\bar{P}}{\bar{\rho}^2}\rho'\rho'^* + \bar{\rho}u_i'u_i'^* + \frac{\bar{P}}{(\gamma-1)\bar{T}^2}T'T'^*\right) \tag{13}$$

where $(.)^*$ denotes complex conjugate and subscript $(.)_i$ denotes the velocity component in the x,y directions. Repeated indices indicate summation. In what follows the total disturbance energy growth rate is referred to as RHS and the constituents are reported normalized by the denominator in Eq. 12 such that at any given x location RHS = P_{tot}+F_{tot}+D_{tot}. Russo et al. [29] showed that extra terms pop out of using the spatial framework for the energy budget analysis but are negligibly small and the simpler Eq. 12 may be used.

A. Total Energy Budgets

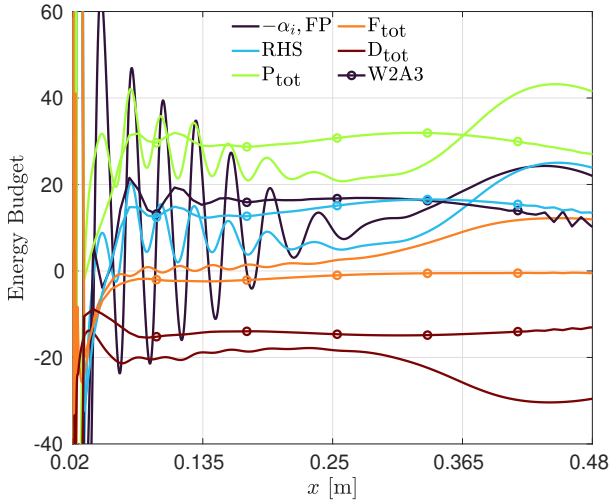

Fig. 6 Total energy budget terms for cases FP (flat plate) and W2A3. Open circles have been added to the curves for the W2A3 results to distinguish them from the FP results.

The production, flux, and dissipation terms were computed for both the FP and W2A3 cases corresponding to their maximum N factor second mode frequencies of $f \approx 120$ kHz and $f \approx 78$ kHz, respectively. Along with the constituents, the total RHS is also plotted in Figure 6. From here onward, unless otherwise stated, all stream-wise curves have been obtained by roughness wavelength (λ_x) averaging the quantities of interest. As a sanity check, the growth rate derived based only on the pressure disturbance amplitude at the wall (α_i) is also included in the plot to verify that the disturbance energy growth rate derived from the energy budget is correct. One can see that for both cases the curves corresponding to α_i (black) and RHS (light blue) are close over the entire stream-wise extent of the domain. Also, this shows another case where the extra terms arising from the spatial framework for energy budget analysis are negligibly small and can be omitted in the present analysis. Several trends jump out immediately from Figure 6, the first being that the total disturbance energy growth rate has a lower (in maximum), broader distribution in the roughness case than the smooth wall. The smooth wall has lower energy growth rate except towards the end of the domain where it surpasses that of the W2A3. We already saw from the N factor curves in Figure 4 that the broadness of the growth rate in the W2A3 case leads to a higher integral N-factor than the shorter taller distribution from the smooth wall case. Since the flux terms (orange) are negligibly small throughout the entire domain considered, the primary cause of second mode destabilization is presumably originating from heightened energy production combined with diminished dissipation over wider spatial extent than the smooth wall case. The plots that follow seek to understand the driving mechanisms of these macroscopic observations.

B. Sub-term Energy Budgets

Before discussing the results of looking at the subtotal energy budget terms, they are briefly enumerated here. First, the production term is comprised of

$$P_{tot} = P_{RS} + P_{mom} + P_{En} + P_{PW} + P_{Dila} + P_{IE} + P_{TP}, \tag{14}$$

where the terms on the right-hand side are production due to work done by disturbance Reynolds stresses on mean velocity gradients, convection of disturbance momentum across mean flow velocity shear, entropy spottiness across temperature shear layer, pressure work, dilatation, internal energy, and transport property variation, respectively. The flux term is comprised of

$$\mathrm{F_{tot}} = \mathrm{F_{TP}} + \mathrm{F_{HF}} + \mathrm{F_{PW}} + \mathrm{F_{SW}}, \tag{15}$$

where the terms on the right-hand side cause energy flux (or redistribution) via transport property variation, heat conduction, pressure work, and shear work, respectively. Lastly, the total dissipation term is comprised of

$$\mathrm{D_{tot}} = \mathrm{D_{HF}} + \mathrm{D_{SW}}, \tag{16}$$

where the terms on the right-hand side dissipate energy through heat conduction and shear work, respectively.

Figure 7 shows the most important of these constituent terms for production, flux, and dissipation. Beginning with the production sub terms (see Figure 7a), the Reynolds stress and entropy energy production terms dominate the total. These terms mathematically read

$$\mathrm{P_{RS}} = -\bar{\rho}\left(u'u'\frac{\partial \bar{u}}{\partial x} + u'v'\frac{\partial \bar{u}}{\partial y} + u'v'\frac{\partial \bar{v}}{\partial x} + v'v'\frac{\partial \bar{v}}{\partial y}\right), \tag{17}$$

and

$$\mathrm{P_{En}} = -\left[\bar{\rho}R_{gas}\left(\frac{T'}{(\gamma-1)\bar{T}} - \frac{\rho'}{\bar{\rho}}\right)\left(u'\frac{\partial \bar{T}}{\partial x} + v'\frac{\partial \bar{T}}{\partial y}\right)\right]. \tag{18}$$

All other terms (shown in gray lines) are much smaller than the Reynolds stress and entropy terms. The significant

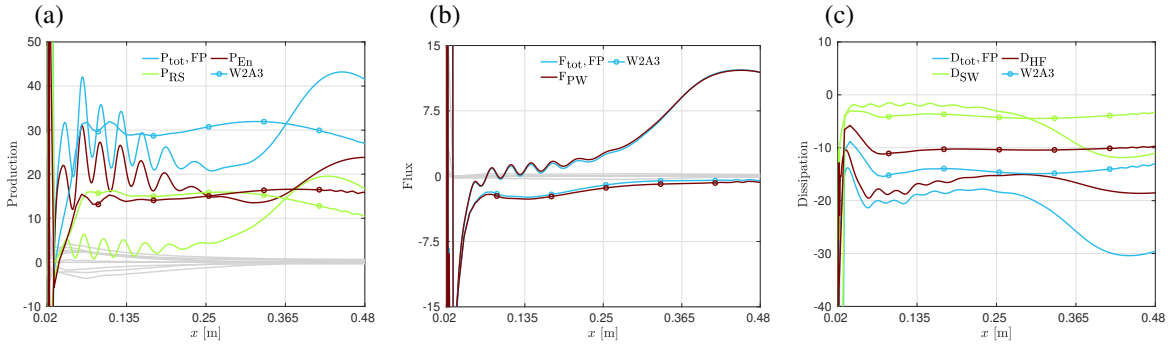

Fig. 7 Sub-budget terms compared between flat plate (FP) and W2A3 roughness for disturbance energy (a) production, (b) flux, and (c) dissipation.

Reynolds stress production for the W2A3 case occurs over nearly the entire domain and is roughly the same magnitude as the entropy term, demonstrating nearly equal contributions from both to the total. The smooth wall case on the other hand has negligibly small Reynolds stress over most of the domain and the dominating production term is always entropy term. The Reynolds stress does pickup towards the end of the domain for the smooth wall where the peak in energy growth rate is achieved. Since both cases have comparable entropy production, it appears already that the destabilization in the roughness case may be caused by a Reynolds stress augmentation introduced somehow through the roughness elements. Moving to the flux sub terms shown in Figure 7b, both cases have energy redistribution mainly contributed by the pressure work mechanism exclusively. This term reads

$$\mathrm{F_{PW}} = -\left[\frac{\partial(u'P')}{\partial x} + \frac{\partial(v'P')}{\partial y}\right]. \tag{19}$$

While the total flux remains low throughout the entire domain for the W2A3 case, the smooth wall has positive flux contributions in the most unstable region that are only about 50% lower than the Reynolds stress production term. As was seen before, the total energy growth rate due to dissipation remains lower (in magnitude, still negative) in the W2A3 case than the FP. These terms are calculated using the following expressions

$$\mathrm{D_{SW}} = -\left[\tau'_{xx}\frac{\partial u'}{\partial x} + \tau'_{yy}\frac{\partial v'}{\partial y} + \tau'_{xy}\left(\frac{\partial v'}{\partial x} + \frac{\partial u'}{\partial y}\right)\right], \tag{20}$$

and

$$\mathrm{D_{HF}} = \frac{1}{\bar{T}}\left(q'_x\frac{\partial T'}{\partial x} + q'_y\frac{\partial T'}{\partial y}\right). \tag{21}$$

The sub-terms not defined here can be found in the Appendix VIII.C. Plotted alongside its constituents, Figure 7c illustrates the fact the dissipation due to heat conduction contributes significantly more to the total dissipation in both cases. While the shear work is slightly more powerful in dissipating energy away in the roughness case (perhaps due to flow separation), the main difference lies in the diminished heat conduction dissipation in the W2A3 case. Thus far, it appears that increased Reynolds stresses and diminished dissipation due to heat conduction play the largest role in the second mode destabilization due to the 2-D roughness. The following section seeks one more level analysis to see why these terms are behaving the way they are.

C. Disturbance Energy Distributions

Through the analyses of the preceding sections we were able to see that the elevated Reynolds stress causes an increase in disturbance energy production over a broad spatial extent for the roughness case. This combined with the diminished dissipation (compared to the smooth wall case) leads to overall higher energy growth. What still is not clear is why these trends occur. To help shed some light on this, the distributions of the dominant terms in energy production and dissipation are shown over two roughness wavelengths of spatial extent. The location selected for consideration corresponded to where the peak total disturbance energy growth occurred for each case, namely $x \approx 0.29$ m and $x \approx 0.44$ m, for the rough and smooth walls, respectively.

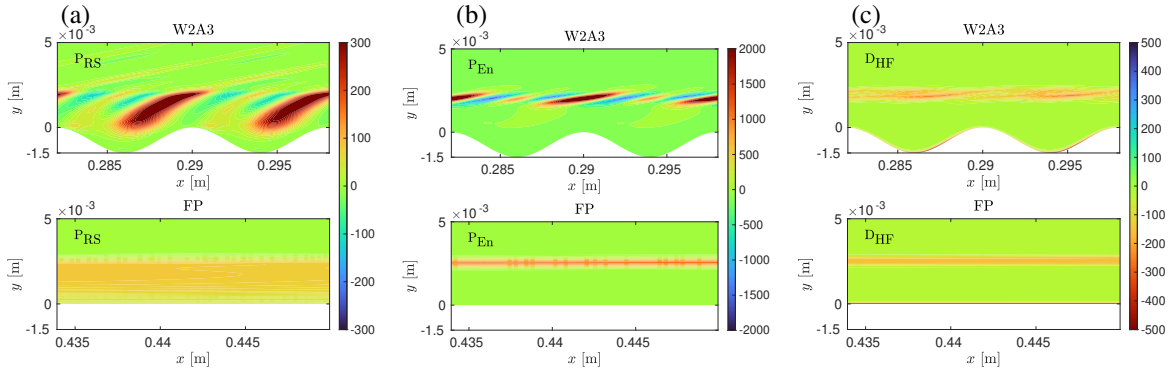

Fig. 8 Spatial distributions of disturbance energy production due to (a) Reynolds stresses and (b) entropy spottiness, and (c) disturbance energy dissipation due to heat conduction, for both W2A3 roughness (top) and smooth wall (bottom).

Starting with the Reynolds stress distributions shown in Figure 8a, a marked difference can be observed between the rough and smooth wall cases. The smooth wall exhibits a nearly uniform distribution in Reynolds stress from low in the boundary layer all the way up to the edge which is expected due to small variation of the flow in streamwise direction. The roughness case, on the other hand, shows a more complicated distribution with much larger peaks in Reynolds stress energy production present at the windward shoulder of the roughness element peaks. Ever so slight negative contributions ensue slightly past the roughness peak, but they cannot cancel out the preceding positive contribution, and the wavelength-averaged growth rate comes out to much larger than the smooth wall case. The main difference between the two flow fields is the presence of the compression-expansion shock wave system occurring over each roughness element peak (illustrated in later figures). This may be causing the elevated Reynolds stress production.

Moving to the entropy production term in Figure 8b, it is evident that the entropy terms are predominantly active within a very narrow region surrounding the critical layer. Again it can be seen that the wavy wall case has a spottier distribution than the smooth wall case. The reader should take note of the varying minimum and maximum values for the color contours. It is about 600% larger than the Reynolds stress plot previously discussed. This was done to appreciate the massive overshoots in entropy production occurring for the wavy wall case near the boundary layer edge over the tops of the roughness peaks. The smooth wall too possess the peak in entropy production near the boundary layer edge, but it is over a shorter wall-normal extent and varies imperceptibly in the stream-wise direction. Heat conduction dissipation shows interesting distributions as well (Figure 8c). Considering that conduction is a much slower physical

process than convection of momentum and thermal fluctuations the D_{HF} term appears to be less affected. The smooth wall case shows peak dissipation at the wall that is significantly larger than the lower peak near the boundary layer edge. Similarly, the W2A3 roughness distribution possesses these two peaks, however, the stream-wise variation is similarly modulated in streamwise direction as the previously discussed production terms. In the roughness case, the dissipation does peak at the wall, but it is restricted to the windward roughness trough and only makes it about half way up the roughness element before diminishing. This combined with the cancellations present near the boundary layer edge result in the integrated decrease in dissipation seen in the previous plots. The cause of this is likely the separation bubble where slow moving fluid over the majority of the roughness wall reduces the near wall flow gradients and the energy dissipation mechanisms there. Other portions of the wall (near the peak) have enhanced shear, however, they occur over a lesser stream-wise extent and the average over the wavelength results in lower dissipation than the smooth wall.

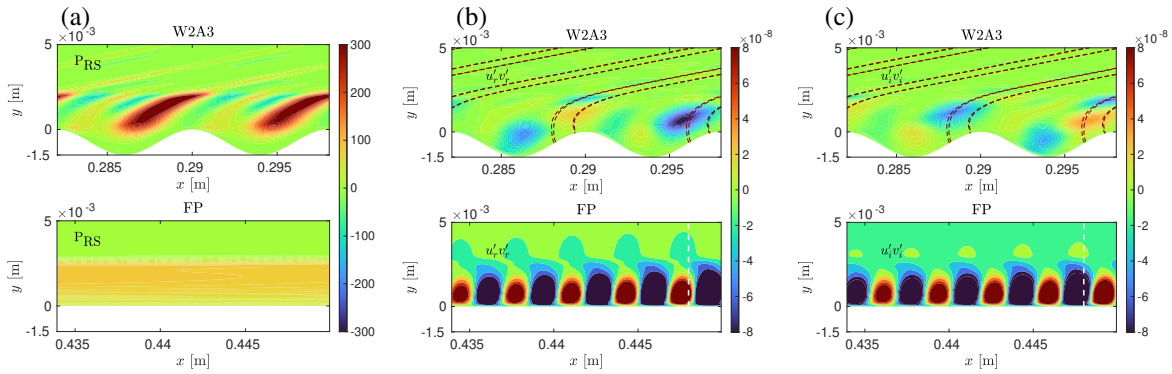

Fig. 9 Spatial distributions of disturbance energy production due to (a) Reynolds stresses, and the products of disturbance velocity real parts (b) and imaginary parts (c), for W2A3 (top) and smooth wall (bottom).

Given that the main difference in energy production between the smooth wall and roughness case lies in the Reynolds stress term, a closer look is taken to help understand why this difference arises. To do this, first recall the terms that comprise the Reynolds stress shown in Eq. 17. The most dominant of the four terms (comparison not shown here) was found to be the second one, denoted RS_2, which contributed almost entirely to the total P_{RS}. Given that this term should be real valued $RS_2 = -\bar{\rho}u'v'\frac{\partial \bar{u}}{\partial y}$, yet the complex product u' and v' yields a complex number (except when $u' = v'^*$), we consider only the real part in the energy budget analysis. Thus, the RS_2 term produces disturbance energy only when $u'_r v'_r + u'_i v'_i < 0$, or the phase difference between the two velocities is $\pm\pi$. Here, the subscript "r" and "i" denote real and imaginary parts of a complex number, respectively. To see where in the flow field these two parts of the summation interfere to become negative/positive or net zero, Figure 9 plots again the Reynolds stress distributions for the W2A3 and smooth case for quick reference. Newly featured are the fields of $u'_r v'_r$ (Figure 9b) and $u'_i v'_i$ (Figure 9c) that contain the outline of the high pressure front formed by the compression wave shown as dashed lines for the wavy case. Only a vertical reference line at the same x location is provided for the smooth wall case given the minimal stream-wise variation in Reynolds stress. By inspection of the velocity product fields for the smooth wall case, even though the peaks are more saturated in the plot, they cancel each other out to a large extent and the result is the more mild Reynolds stress seen on the left. This is verified by considering the largely negative $u'_i v'_i$ near the vertical dashed line in Figure 9c and the smaller (magnitude) positive lobe at the same dashed line in Figure 9b for $u'_r v'_r$, thus yields a small negative number and a small positive Reynolds stress production term. On the other hand, the rough wall fields exhibit smaller extrema in $u'_r v'_r$ and $u'_i v'_i$, but in regions sloping up the windward side of a roughness element they are very nearly out of phase and contribute largely to the Reynolds stress. The main flow field structure that could cause this increase in phase shift is the compression-expansion shock wave system present for the wavy wall. Thus, it can be concluded that the Reynolds stress energy production is increased in the rough wall case due to compression waves emanating from the roughness elements.

VII. Extension to 3-D

Up until this point, all calculations discussed have been performed in two spatial dimensions (x,y) using 2-D sinusoidal roughness shapes. This can be thought of a special case of the real-world situation faced by hypersonic vehicles where surface roughness varies both in the stream- and span-wise directions (presumably randomly as well). The preliminary work presented here seeks to incorporate some of these realities in the simulation by utilizing a 3-D

sinusoidal roughness distribution with random phasing in span.

A. Steady Flow Field

Using again the roughness parameters defined for the W2A3 case, first a steady solution was obtained over the flat plate with 3-D surface roughness. Similar as in 2-D for the stream-wise direction, 20 cells were used to resolve each roughness element in the span, which extended six wavelengths (i.e., $z \in [0, 6\lambda_x]$). Figure 10 visualizes the steady flow field computed over the flat plate with 3-D roughness. Cross-plane slices near the end of the domain ($x \approx 0.4$) of stream-wise velocity shown on the left illustrate the dramatic effects of including span-wise varying surface roughness on the steady solution. The momentum deficit created by the increased pressure on the roughness element windward side results in the lower velocity fluid that gets transported upward by the lift-up effect [32]. These oscillations of high and low speed fluid in the span-wise direction are commonly referred to as velocity "streaks." It is interesting to note that the peaks of these streaks, while still exhibiting the wavelength of the roughness elements, wanders to the right as one follows them from cross-plane to cross-plane in the downstream direction. This indicates that while the phasing applied to the roughness elements are randomized, the distribution is such that it favors slightly the introduction of span-wise velocity to the right. This is confirmed by the cross-plane contours of span-wise velocity shown to the right in Figure 10 where even though negative and positive span-wise velocity lobes straddle the roughness elements close to the wall (as fluids gets parted by the obstacle), farther away from the wall shows positive (red) span-wise velocity causing the wandering of the streaks previously noted. This net cross-flow vortex system is reminiscent of that obtained by Stemmer et al. [33] when simulating a pseudo-randomized roughness patch on the surface of a blunt body at hypersonic speeds. Such strong span-wise gradients in stream-wise velocity provide ripe conditions for wake instabilities of the

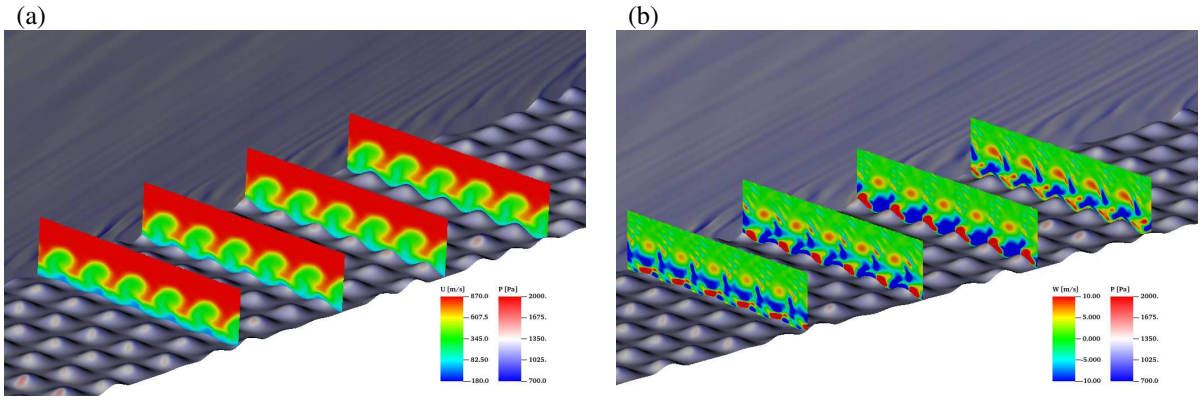

Fig. 10 Steady flow field visualization for case W2A3 with randomized surface roughness phasing in 3-D. Surface and x-y plane colored by pressure and cross-plane (z-y) colored by stream-wise velocity (a) and span-wise velocity (b).

type shown for isolated roughness and the relevance of second mode instability in this case may come into question. The next subsection investigates this question.

B. Pulse Simulation Results

Given that the flow field becomes highly three-dimensional once the surface roughness is allowed to vary in the span-wise direction, again a pulse disturbance was introduced into the steady field to assess whether or not the second mode is still relevant for transition in this case. This pulse was two-dimensional (with no span-wise variation) to keep the comparison with the aforementioned pulse simulations performed in two spatial dimensions as fair as possible. It will be the subject of future work to analyze the response to a 3-D pulse like the one used in Ref. [18].

Probes distributed over the wall recorded the temporal signal and then were used to project the disturbances onto the span-wise wavenumber-temporal frequency domain. Looking at this space at select x locations, as is done in Figure 11, one can gain insight into the spatial and temporal length scales being amplified in the wave packet. At $x = 0.15$ m (Figure 11a) the spectra shows the 2-D modes ($\beta/\beta_k = 0$) has the highest disturbance amplitude in the range $f \in [25, 50]$ kHz. This frequency range is also excited for the span-wise wavenumber introduced by the roughness elements, β_k, and their harmonics but to a lesser extent. Moving downstream to $x = 0.25$ m (Figure 11b) one can see that the 2-D modes are

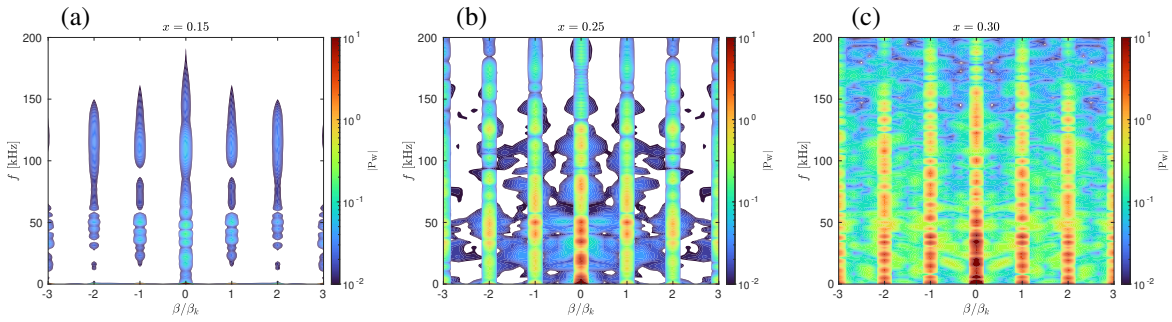

Fig. 11 Wall pressure frequency-spanwise wavenumber spectra at (a) $x = 0.15$ m, (b) $x = 0.025$ m, and (c) $x = 0.30$ m, obtained from the 3-D W2A3 pusle simulation.

still dominating the flow field despite it's high three-dimensionality. Highest amplitude frequencies remain between $f = 25$ kHz and $f = 60$ kHz, but the modulated streaks are seeing amplification as well (e.g., $(f, \beta/\beta_k) = (50\text{kHz}, 1)$). The interaction of 2-D modes with 3-D streaks has also been observed in simulations of 3-D roughness on a cylinder surface under subsonic post-shock conditions, as reported by Braga *et al.* [14]. Additionally, these cylinder simulations also showed the emergence of spottiness in the spectra, which was attributed to phase randomization between the rows of roughness elements in the spanwise direction. The spectra showed much more coherent structures are present for perfectly staggered or aligned roughness elements. Finally, by $x = 0.30$ m, the spectrum fills up and the flow appears to be well on its way to turbulence. These trends are more easily visualized in Figure 12 where the N factor for each mode is plotted as they evolve in the downstream direction. Only the $(f, \beta/\beta_k) = (25\text{kHz}, 0)$ mode from the 3-D calculation is plotted in color (light blue) since this one was shown to be dominant in the $\beta - f$ spectra. Other gray lines intermittently surpass this frequency's N factor but also belong to the 2-D modes within the frequency range highlighted in the spectra. Also plotted are the N factor envelopes obtained from the 2-D LNSE calculations highlighted previously. In this way, it is evident that the 3-D roughness destabilizes the flow even more than the 2-D roughness at the same roughness parameters (W2A3). Indeed, it is destabilized more than any of the 2-D rough walls analyzed, but the initial growth rate is not incredibly higher than that of case W2A1 for $x < 0.2$ m. It should also be noted that the amplified frequency band became even more broad, a trend that is a continuation from 2-D (see spectra in Figure 3). Seeing 2-D $(\beta - 0)$ modes achieving similar growth rates in a 3-D calculation (over some spatial extent) gives merit to the idea of possibly being able to find a 2-D equivalent surface roughness for which stability calculations could be performed at significant fractions of the computational cost. Future work will introduce a pulse disturbance with a range of spatial length scales to determine whether the 2-D modes seen here remain most amplified. Furthermore, we will examine the amplitude distributions corresponding to various frequency and wavenumber pairs to gain deeper insights into the distinct instability mechanisms that are excited.

VIII. Conclusions

This work examined 2-D and 3-D effects of distributed sinusoidal roughness on the boundary layer stability at Mach 5.35 over a flat plate. For 2-D, the introduction of roughness elements with increasing height resulted in more significant flow separation in the roughness troughs, as well as stronger compression-expansion shock systems to form in the steady state flow field. Disturbances introduced to this boundary layer flow were analyzed to investigate how the distributed surface roughness destabilized the dominant Mack second mode across an increasingly broad range of frequencies. In addition to the second mode, Mack's third mode became destabilized in the case of larger roughness height. LST used in previous work for mode identification [16] was again utilized and found to predict the growth rate of disturbances over the rough wall fairly well. An energy budget analysis revealed significant differences in the disturbance energy production for the rough wall case W2A3, namely a marked increase in Reynolds stress energy production at the same time as milder heat conduction disturbance energy dissipation. The decrease in dissipation was attributed to the significant flow separation over the roughness troughs, and the increase in Reynolds stresses were seen to arise from the compression-expansion shock system that forms over the peaks of the roughness elements. Simulations were then performed over randomly phased (in span) distributed sinusoidal roughness in 3-D to investigate whether trends observed in 2-D were applicable to the more realistic scenario of 3-D roughness. The steady flow field over this roughness pattern exhibited very strong velocity streaks that seemed to follow an induced span-wise velocity to

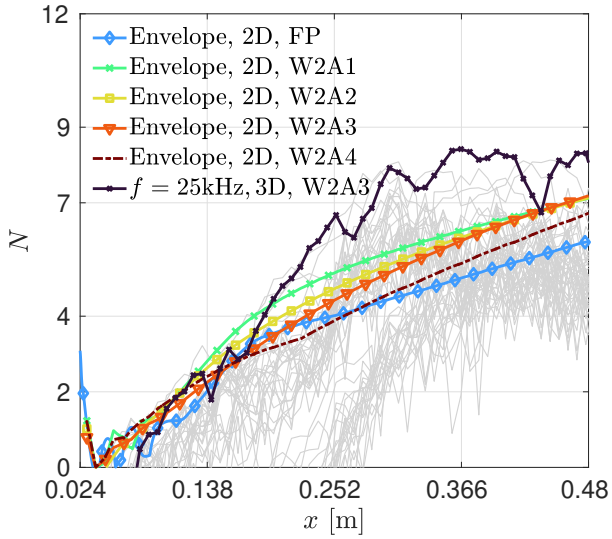

Fig. 12 N factor curves for W2A3 roughness in 3-D, and N factor envelopes for all 2-D cases considered.

the right. 2-D pulse simulation on this steady flow field revealed higher and broader frequency amplification than the corresponding 2-D roughness case. Future work aims to more closely examine the mechanism responsible for the heightened amplification when moving from 2-D to 3-D roughness.

Appendix

A. Grid Convergence

The initial wall-normal grid spacing was decreased from the nominal $\Delta y_w = 8$ μm to $\Delta y_w = 5$ μm at the same time as the wall-normal cell count was increased from 400 to 500. Figure 13 below demonstrates the results for second mode growth at 78 kHz for the W2A3 case remain very similar. Growth rate shows minor differences toward the end of the domain.

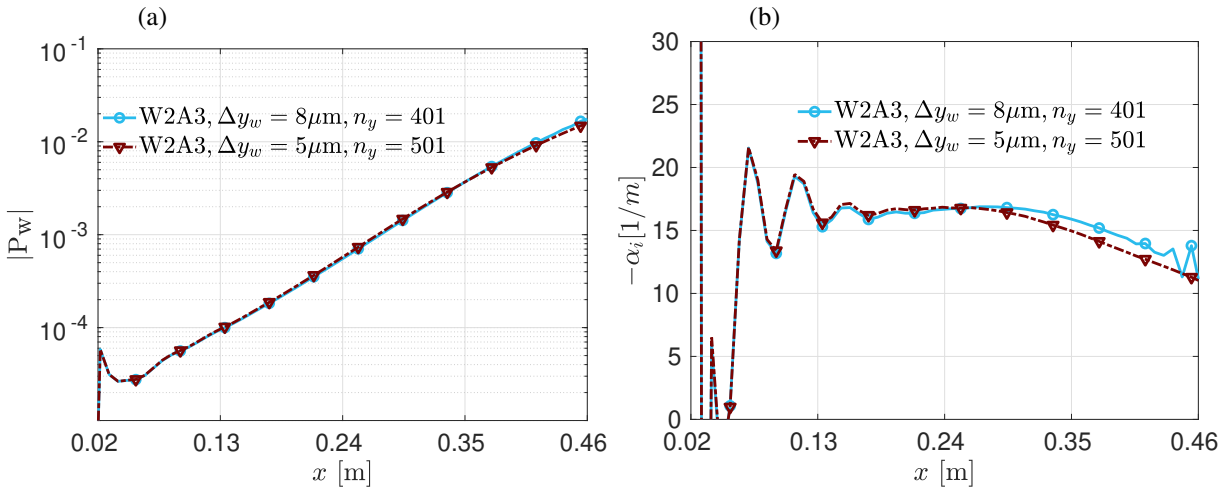

Fig. 13 Amplitude (a) and growth rate (b) shown for f = 78 kHz disturbances using variable wall spacing and cell count.

B. Roughness Invariance

The following plots verify the previously made claim that the growth rate of second mode disturbances over the distributed roughness is invariant to whether the roughness elements are generated by displacing the wall downward or upward. The amplitude on the other hand is not invariant, which can be seen in Figure 14 where the roughness displaced upward achieves a lower amplitude at the position of neutral stability ($x \approx 0.05$ m) as compared to the solution obtained on the roughness elements displaced downward. This result is likely caused by the separation bubble formed at the beginning of the first roughness element. Note, these results are for 2-D roughness elements.

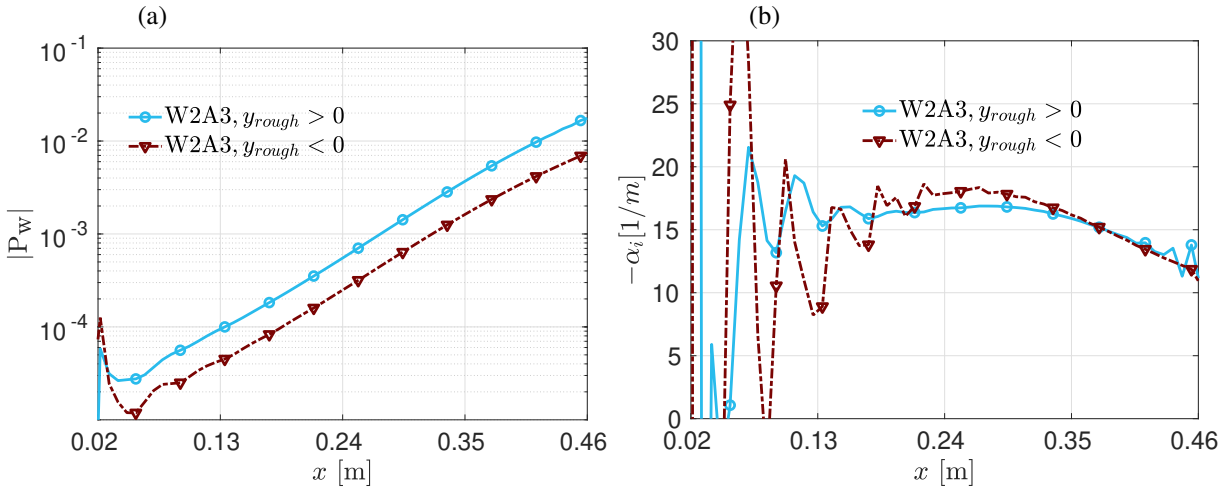

Fig. 14 Amplitude (a) and growth rate (b) shown for $f = 78$ kHz disturbances using roughness displaced upward ($y_{rough} > 0$) and downward ($y_{rough} < 0$).

C. Addition Energy Dissipation Terms

These terms are present in the energy dissipation equation due to shear work and heat conduction but their definition was saved until now for the sake of brevity. Note, $\lambda = -\frac{2}{3}\mu$ following Stoke's hypothesis.

$$q'_x = -\bar{\kappa}\frac{\partial T'}{\partial x} \qquad q'_y = -\bar{\kappa}\frac{\partial T'}{\partial y}$$

$$\tau'_{xx} = (2\bar{\mu} + \bar{\lambda})\frac{\partial u'}{\partial x} + \bar{\lambda}\frac{\partial v'}{\partial y} \qquad \tau_{yy} = (2\bar{\mu} + \bar{\lambda})\frac{\partial v'}{\partial y} + \bar{\lambda}\frac{\partial u'}{\partial x}$$

$$\tau_{xy} = \bar{\mu}\left(\frac{\partial u'}{\partial y} + \frac{\partial v'}{\partial x}\right)$$

Acknowledgments

The authors extend their sincere gratitude for the financial support provided by the NDSEG fellowship program and the National Science Foundation under award number CBET-2146100, with Dr. R. Joslin serving as Program Manager.

References

[1] van Driest, E., "The problem of aerodynamic heating," *Aeronautical Engineering Review*, Vol. 15, 1956, pp. 26–41.

[2] Hader, C., and Fasel, H. F., "Direct numerical simulations of hypersonic boundary-layer transition for a flared cone: fundamental breakdown," *Journal of Fluid Mechanics*, Vol. 869, 2019, p. 341–384. https://doi.org/10.1017/jfm.2019.202.

[3] Padilla Montero, I., and Pinna, F., "Analysis of the instabilities induced by an isolated roughness element in a laminar high-speed boundary layer," *Journal of Fluid Mechanics*, Vol. 915, 2021, p. A90. https://doi.org/10.1017/jfm.2021.70.

[4] Wheaton, B. M., and Schneider, S. P., "Roughness-Induced Instability in a Hypersonic Laminar Boundary Layer," *AIAA Journal*, Vol. 50, No. 6, 2012, pp. 1245–1256. https://doi.org/10.2514/1.J051199.

[5] De Tullio, N., Paredes, P., Sandham, N. D., and Theofilis, V., "Laminar–turbulent transition induced by a discrete roughness element in a supersonic boundary layer," *Journal of Fluid Mechanics*, Vol. 735, 2013, p. 613–646. https://doi.org/10.1017/jfm.2013.520.

[6] Choudhari, M., Li, F., and Edwards, J., *Stability Analysis of Roughness Array Wake in a High-Speed Boundary Layer*, 2009. https://doi.org/10.2514/6.2009-170.

[7] Van den Eynde, J. P. J. P., and Sandham, N. D., "Numerical Simulations of Transition due to Isolated Roughness Elements at Mach 6," *AIAA Journal*, Vol. 54, No. 1, 2016, pp. 53–65. https://doi.org/10.2514/1.J054139.

[8] Floryan, J., "Stability of wall-bounded shear layers in the presence of simulated distributed surface roughness," *Journal of Fluid Mechanics*, Vol. 335, 1997, pp. 29–55.

[9] Brehm, C., Dackermann, T., Grygier, F., and Fasel, H., "Numerical investigations of the influence of distributed roughness on Blasius boundary layer stability," *49th AIAA Aerospace Sciences Meeting including the New Horizons Forum and Aerospace Exposition*, 2011, p. 563. https://doi.org/doi.org/10.2514/6.2011-563.

[10] Saikia, B., Dueñas, L., Dotzauer, N., and Brehm, C., *Effect of Parametric Variation of Sinusoidal Surface Roughness on High-Speed Boundary Layer Stability*, 2021. https://doi.org/10.2514/6.2021-2705.

[11] Saikia, B., and Brehm, C., *Effect of Distributed Surface Roughness on the Stability of High-Speed Flows.*, 2022. https://doi.org/10.2514/6.2022-1212.

[12] Saikia, B., and Brehm, C., *Effects of Distributed Surface Roughness on Supersonic Boundary Layer Receptivity Mechanisms*, 2022. https://doi.org/10.2514/6.2022-4101.

[13] Chou, A., Paredes, P., Kegerise, M. A., King, R. A., Choudhari, M., and Li, F., "Transition induced by an egg-crate roughness on a flat plate in supersonic flow," *Journal of Fluid Mechanics*, Vol. 948, 2022, p. A27. https://doi.org/10.1017/jfm.2022.510.

[14] Braga, M. A., Dungan, S., Brehm, C., and Macdonald, R. L., *Numerical Simulation of Boundary Layer Transition on Mach 6 Cylinder with Randomly Phased Sinusoidal Roughness*, 2024. https://doi.org/10.2514/6.2024-1976.

[15] Hollis, B. R., "Blunt-Body Entry Vehicle Aerothermodynamics: Transition and Turbulent Heating," *Journal of Spacecraft and Rockets*, Vol. 49, No. 3, 2012, pp. 435–449. https://doi.org/doi:10.2514/1.51864.

[16] Saikia, B., and Brehm, C., "On the stability characteristics of a hypersonic boundary layer flow over parameterised sinusoidal surface roughness," *Journal of Fluid Mechanics (under review)*, 2025.

[17] H. Tannehill, R. P., D. Anderson, *Computational Fluid Mechanics and Heat Transfer*, Taylor and Francis, 1997.

[18] Browne, O. M., Haas, A. P., Fasel, H. F., and Brehm, C., "A nonlinear compressible flow disturbance formulation for adaptive mesh refinement wavepacket tracking in hypersonic boundary-layer flows," *Computers & Fluids*, Vol. 240, 2022, p. 105395.

[19] Haas, A. P., Browne, O. M., Fasel, H. F., and Brehm, C., "A time-spectral approximate Jacobian based linearized compressible Navier-Stokes solver for high-speed boundary-layer receptivity and stability," *Journal of Computational Physics*, Vol. 405, 2020, p. 108978. https://doi.org/https://doi.org/10.1016/j.jcp.2019.108978.

[20] McQuaid, J. A., and Brehm, C., "Heat flux predictions for hypersonic flows with an overset near body solver on an adaptive block-structured Cartesian off-body grid," *Computers & Fluids*, Vol. 269, 2024, p. 106121. https://doi.org/10.1016/j.compfluid.2023.106121.

[21] Brehm, C., Barad, M. F., Housman, J. A., and Kiris, C. C., "A comparison of higher-order finite-difference shock capturing schemes," *Computers & Fluids*, Vol. 122, 2015, pp. 184–208. https://doi.org/10.1016/j.compfluid.2015.08.023.

[22] Mack, L. M., "Boundary-Layer Linear Stability Theory," Tech. rep., Jet Propulsion Laboratory, California Institute of Technology, 1984.

[23] Kuehl, J. J., "Thermoacoustic Interpretation of Second-Mode Instability," *AIAA Journal*, Vol. 56, No. 9, 2018, pp. 3585–3592. https://doi.org/10.2514/1.J057015.

[24] Caillaud, C., Esquieu, S., Scholten, A., Paredes, P., Li, F., Choudhari, M. M., Kuehl, J., Lugrin, M., Benitez, E. K., Borg, M. P., McDaniel, Z. A., and Jewell, J. S., *Separation and Transition on a Cone-Cylinder-Flare: Computational Investigations*, 2024, p. 0497. https://doi.org/10.2514/6.2024-0497.

[25] van Ingen, J., "A suggested semi-empirical method for the calculation of the boundary layer transition region," 1956. URL https://api.semanticscholar.org/CorpusID:118788950.

[26] TUMIN, A., "Three-dimensional spatial normal modes in compressible boundary layers," *Journal of Fluid Mechanics*, Vol. 586, 2007, p. 295–322. https://doi.org/10.1017/S002211200700691X.

[27] Herbert, T., "Parabolized Stability Equations," *Annual Review of Fluid Mechanics*, Vol. 29, 1997, pp. 245–283. https://doi.org/https://doi.org/10.1146/annurev.fluid.29.1.245.

[28] Chang, C.-L., "Langley Stability and Transition Analysis Code (LASTRAC) Version 1.2 User Manual," Tech. rep., National Aeronautics and Space Administration, 2004.

[29] Russo, V., Saikia, B., and Brehm, C., *Stability Investigation of High Enthalpy Boundary Layer Flow With Gas Injection Using Energy Budget Analysis*, 2024, p. 4061. https://doi.org/10.2514/6.2024-4061.

[30] Chu, B., "On the energy transfer to small disturbances in fluid flow (Part I)," *Acta Mechanica*, 1965.

[31] Hanifi, A., Schmid, P. J., and Henningson, D. S., "Transient growth in compressible boundary layer flow," *Physics of Fluids*, Vol. 8, No. 3, 1996, pp. 826–837. https://doi.org/10.1063/1.868864.

[32] Brandt, L., "The lift-up effect: The linear mechanism behind transition and turbulence in shear flows," *European Journal of Mechanics - B/Fluids*, Vol. 47, 2014, pp. 80–96. https://doi.org/https://doi.org/10.1016/j.euromechflu.2014.03.005, enok Palm Memorial Volume.

[33] Ulrich, F., and Stemmer, C., "Investigation of vortical structures in the wake of pseudo-random roughness surfaces in hypersonic reacting boundary-layer flows," *International Journal of Heat and Fluid Flow*, Vol. 95, 2022, p. 108945. https://doi.org/https://doi.org/10.1016/j.ijheatfluidflow.2022.108945.